Unit−Cell Approximation for Diblock −Copolymer Brushes Grafted to Spherical Particles

3 AUTHORS, INCLUDING:

Bart Vorselaars
University of Lincoln

18 PUBLICATIONS   **272** CITATIONS

SEE PROFILE

Mark W Matsen
University of Waterloo

134 PUBLICATIONS   **7,829** CITATIONS

SEE PROFILE

Unit-Cell Approximation for Diblock−Copolymer Brushes Grafted to Spherical Particles

G. H. Griffiths,* B. Vorselaars, and M. W. Matsen*

School of Mathematical and Physical Sciences, University of Reading, Whiteknights, Reading, RG6 6AX, United Kingdom

ABSTRACT: This paper examines the equilibrium phase behavior of thin diblock-copolymer films tethered to a spherical core, using numerical self-consistent field theory (SCFT). The computational cost of the calculation is greatly reduced by implementing the unit-cell approximation (UCA) routinely used in the study of bulk systems. This provides a tremendous reduction in computational time, permitting us to map out the phase behavior more extensively and allowing us to consider far larger particles. The main consequence of the UCA is that it omits packing frustration, but evidently the effect is minor for large particles. On the other hand, when the particles are small, the UCA calculation can be readily followed up with the full SCFT, the comparison to which conveniently allows one to quantitatively assess the effect of packing frustration.

INTRODUCTION

Researchers are now making significant progress in patterning surfaces by attaching films composed of immiscible polymers. This generally involves either brushes of two different homopolymers[1−6] or of diblock copolymers.[7−11] In both cases, the general incompatibility of the two chemical components causes the films to develop surface patterns, typically involving arrays of either dots, holes, or stripes. An important advantage of tethering the chains to the surface is that it produces robust films capable of withstanding significant external influences, thus opening up the opportunity for environmentally responsive patterns.[12−14] The initial experiments focused on coating planar surfaces, but there is now a growing interest in patterning spherical particles with either mixed brushes[15−20] or block copolymer brushes.[21]

There already exists a considerable number of calculations[22−27] and simulations[28−33] for planar surfaces to guide the experimental activity. Of the different theoretical approaches, self-consistent field theory (SCFT)[34,35] is particularly useful because it is a full microscopic mean-field theory which can be implemented very efficiently for flat films. Unfortunately, its extension to spherical particles becomes computationally demanding because of the loss in periodic symmetry. As a result, many SCFT studies have restricted their attention to special low-dimensional cases, such as uniform phases where the morphology has no angular dependence[36] or by simply ignoring the radial dependence of the problem.[37−39] The first full 3D SCFT calculation was performed by Roan[40,41] for mixed brushes, but his numerical algorithm was so computationally demanding that it would generally require days of CPU time to obtain a single self-consistent solution. Very recently, Vorselaars et al.[42] devised a far more efficient algorithm which they applied to diblock-copolymer brushes. Their method reduces the computational cost by about 2 orders of magnitude, allowing solutions to be obtained in less than an hour. Even though this represents a huge improvement, it still remains a demanding task to map out equilibrium phase diagrams. Furthermore, such times

are only achievable for small particles, where the radius of the core, R_c, is of similar size to the thickness of the polymer film, L. Because the CPU time scales as $LR_c^3 \ln(R_c)$, the calculation quickly become unmanageable for large particles.[43]

Here we sacrifice some of the accuracy of a full SCFT calculation in order to significantly reduce the computational cost. For this, we turn to the unit-cell approximation (UCA) introduced by Helfand and Wasserman over 30 years ago to study the spherical[44] and cylindrical[45] phases of bulk diblock-copolymer melts. It is now a well tried and tested approximation routinely used for bulk systems.[46−49] The same opportunity exists for the dot and hole morphologies commonly observed in structured films. Using it, we investigate the system illustrated in Figure 1 involving diblock−copolymer brushes grafted to a spherical core.

THEORETICAL METHOD

Our study considers the exact same system examined previously by Vorselaars et al.,[42] where AB diblock copolymers are grafted by their B ends to a spherical core of radius R_c, forming a thin polymer melt of uniform thickness L (see Figure 1). The spatial dimensions are all measured in terms of the natural end-to-end length of the diblock chains, $aN^{1/2}$, where a is the statistical segment length and N is the number of segments per chain, of which a fraction f forms the A block. The incompatibility of the A and B segments, controlled by the usual Flory−Huggins χ parameter, creates an interfacial tension between A- and B-rich domains. Our assumption that the polymer film has a uniform thickness (i.e., a spherical air surface) requires the A/B interfacial tension to remain small relative to the surface tension with the air. It would be straightforward to include surface affinities at the inner and outer edges of the film,[27] but we assume both the core
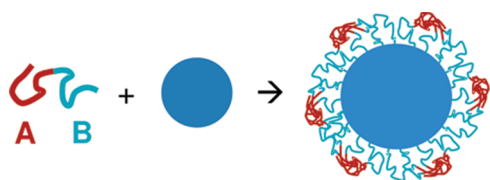
Figure 1. Chemically patterned nanoparticle formed by grafting a thin film of AB diblock copolymer to a spherical core.
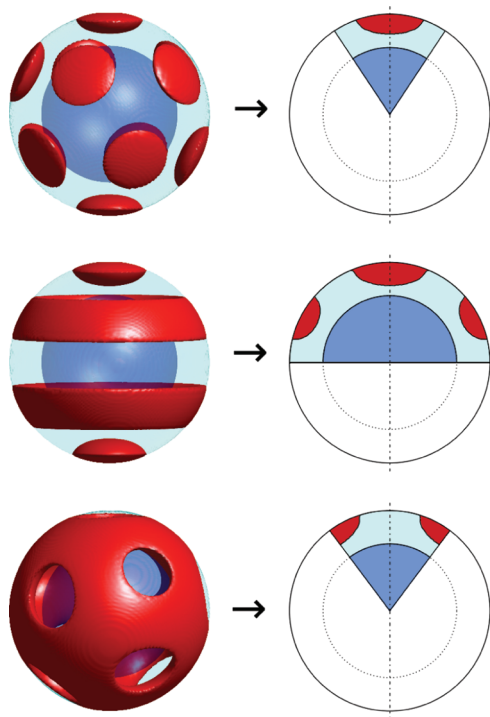

Figure 2. 12-dot, 4:3-stripe and 10-hole phases calculated with the full 3D SCFT (left), and the unit cells used in the present SCFT calculation (right). The A-rich domains are colored red, the B-rich domains are light blue, and the core is dark blue. A/B interfaces are defined by the locus of points where the A- and B-segment concentrations are equal.

and the air are neutral with respect to the A and B components, so as to maintain a more manageable parameter space.

The calculation for a flat substrate $(R_c \rightarrow \infty)$[27] predicts a simple uniform phase plus three phases with lateral structure, where the A-rich domains form a hexagonal array of dots, a series of stripes, or a layer with a hexagonal array of holes. For spherical substrates,[42] the structured phases can still be classified as dot, stripe, and hole morphologies. However, on account of the finite surface area, $A = 4\pi(R_c + L)^2$, each of the morphologies undergoes discontinuous phase transitions as the number and thus size of the dots, stripes, or holes varies. We label the different dot (or hole) phases by an integer, n, specifying the total number of dots (or holes), and for the stripe phases, we use a set of two integers, $m:n$, where m and n denote the number of distinct A- and B-rich surface domains, respectively. Figure 2 shows the morphologies for the 12-dot, 4:3-stripe, and 10-hole phases, calculated using the full SCFT.[42]

Figure 2 also demonstrates how the unit-cell approximation (UCA) is applied in order to speed up the SCFT calculation. Analogous to the application for bulk morphologies,[44−49] we assume that each dot (or hole) of the n-dot (or n-hole) phase
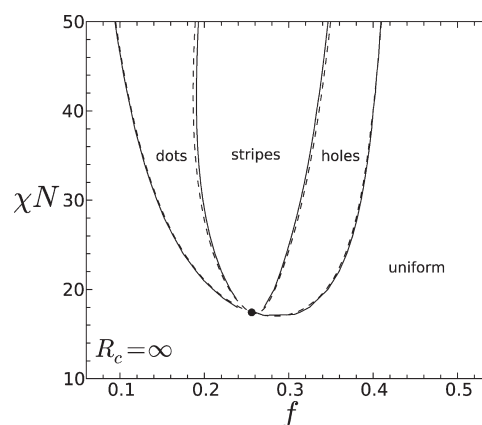

Figure 3. Phase diagram for diblock-copolymer brushes grafted to a flat substrate $(R_c = \infty)$, calculated with (solid curve) and without (dashed curves) the UCA. The dot denotes a mean-field critical point.

occupies a circular unit cell spanning a solid angle of $4\pi/n$. Not only does this reduce the volume over which the calculation is performed by a factor of n, it also introduces a rotational symmetry thus transforming the problem to a 2D calculation. Furthermore, we limit our attention to stripe phases with rotational symmetry (like the one shown in Figure 2) so that they are also 2D calculations. For $m:n$-stripe phases with $m = n \pm 1$, the morphology is symmetric about the equator and so in these cases it is sufficient to perform the calculation over one hemisphere.

The SCFT for this system has already been well described,[27,42] and so we will just outline our numerical algorithm, which can be divided into two parts. The first part calculates the segment concentrations for given fields, which requires us to solve a modified diffusion equation for partial partition functions with Neumann boundary conditions along all surfaces of the unit cell. This is done using the Crank-Nicolson algorithm on a real-space mesh in spherical-polar coordinates, (r, θ, φ). The radial coordinate spans the range $R_c \leq r \leq R_c + L$, while the polar coordinate varies over $0 \leq \theta \leq \theta_{max}$, where $\cos(\theta_{max}) = 1 - 2/n$ for dots or holes and $\theta_{max} = \pi/2$ or π for stripes. The azimuthal angle, φ, simply drops out of the problem because of the rotational symmetry. Our implementation follows a previous SCFT calculation by Kim and Matsen,[50] except that we replace the usual finite-difference approximation for the radial part of the Laplacian by a finite-volume approximation,[42,49] which improves the conservation of polymer. Because the resulting algorithm is so fast, we can afford to use an exceptionally fine mesh (e.g., a grid spacing of $0.01aN^{1/2}$ in the spatial dimensions and 500 points along the chain contour) to absolutely ensure that the numerical inaccuracy is irrelevant. The second part of the SCFT calculation adjusts the fields so as to satisfy self-consistency. This is done iteratively with the Anderson-mixing algorithm as implemented by Matsen,[51] which converges so rapidly that we can afford to enforce an extra-stringent error tolerance for the self-consistent field conditions.

■ RESULTS

Even with our assumptions of neutral air and core surfaces and of uniform film thickness, the behavior of the brush is still controlled by four quantities: $L/aN^{1/2}$, $R_c/aN^{1/2}$, χN, and f. For this study, we only vary the latter three with the film
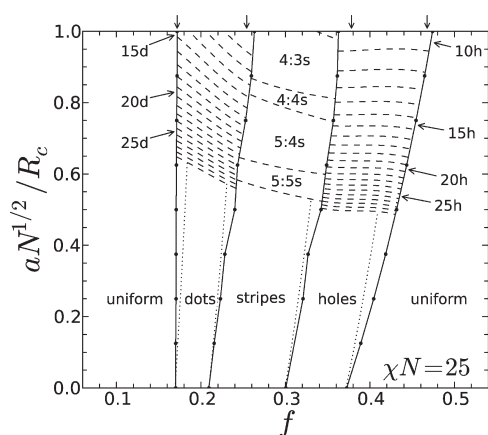
Figure 4. Phase diagram for a fixed segregation of $\chi N = 25$. Solid curves represent the boundaries between the four morphology classes: uniform, dots, stripes and holes. At large R_c, these boundaries are compared to the dotted curves obtained from eq 1. The arrows at the top denote the boundaries calculated by Vorselaars et al.[42] for $R_c = aN^{1/2}$ without the UCA. For small R_c, transitions in the number of surface domains are plotted with dashed curves.

Figure 5. Phase diagram for diblock copolymers grafted to a spherical core of radius $R_c = aN^{1/2}$. The n-dot, m:n-stripe, and n-hole morphology types are separated by solid curves, while the transitions in m and n are marked by dashed curves. The dotted curve denotes a discontinuous transition where A-rich domains jump into contact with the substrate.

thickness fixed at $L/aN^{1/2} = 0.5$. We begin by plotting a phase diagram in Figure 3 for the limit of a flat substrate ($R_c \rightarrow \infty$), where the unit cells of the dot and hole phases are approximated by circular cylinders. Because the substrate has an infinite surface area, there is no constraint on the size of the unit cells and therefore they are adjusted so as to minimize the free energy. We also plot the phase boundaries from the full SCFT calculation with the proper hexagonal unit cells (dashed curves),[27] which allows us to test the validity of the UCA. As we can clearly see, very little accuracy is sacrificed by implementing the UCA in the large-R_c limit.

We now turn our attention to curved substrates and plot the phase boundaries as a function of f and R_c^{-1} at fixed $\chi N = 25$ in Figure 4. The phase diagram still contains the same four types of morphology (i.e., uniform, dot, stripe, and hole phases) separated by the solid curves. The general shift of the phase boundaries toward larger composition f with decreasing particle size, R_c, is largely attributed to the fact that the area of polymer film expands as $4\pi(R_c + z)^2$ with increasing distance, z, from the grafting surface. Following this rational, Vorselaars et al.[42] suggested that the morphology of a flat brush with composition, f, would approximately map onto that of a spherical brush with an effective composition

$$f_{eff} = \frac{4\pi}{V A_{cell}} \int_{cell} \phi_A^{flat}(\mathbf{r})(R_c + z)^2 \, d\mathbf{r} \tag{1}$$

where the A-segment concentration in the flat brush, $\phi_A^{flat}(\mathbf{r})$, is integrated over one unit cell of area A_{cell}. The quantity $V = 4\pi((R_c + L)^3 - R_c^3)/3$ is the total volume of polymer. With this mapping, one can transform the phase boundaries of the flat-brush system to those of the spherical-brush system. Although the two phases at the boundary give slightly different values of f_{eff}, the difference is small and so we just take the average value. The resulting boundaries, obtained from our UCA for $\phi_A^{flat}(\mathbf{r})$, are shown with dotted curves in Figure 4. The mapping does capture the correct trend, but becomes increasingly inaccurate for small particles.

Unlike for the infinite flat brush, the air surface of a spherical brush has a finite area, $A = 4\pi(R_c + L)^2$, and thus any change
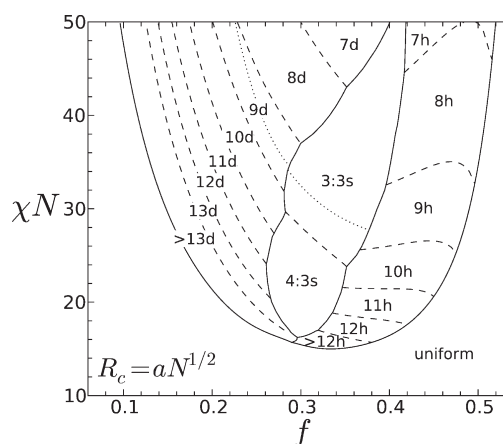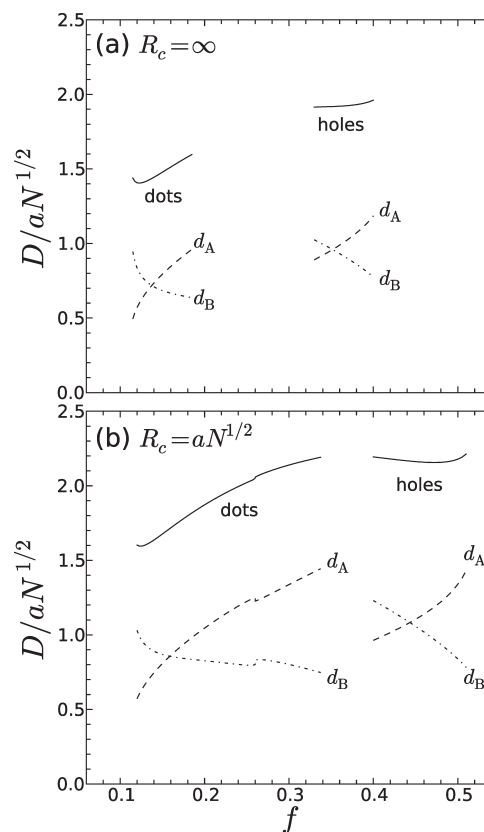

Figure 6. Preferred domain size, $D = d_A + d_B$, of the dot and hole phases calculated as a function of f at $\chi N = 40$ for (a) flat and (b) spherical substrates. The widths of the A- and B-rich domains, d_A and d_B, are shown with dashed and dashed—dotted curves, respectively.

in the number of surface domains results in a discontinuous phase transition. The spacing between these transitions (dashed curves in Figure 4) become very narrow for large particles, and therefore they are only plotted for small R_c. The phase diagram in Figure 4 extends down to a radius of $R_c = aN^{1/2}$, which is the core size
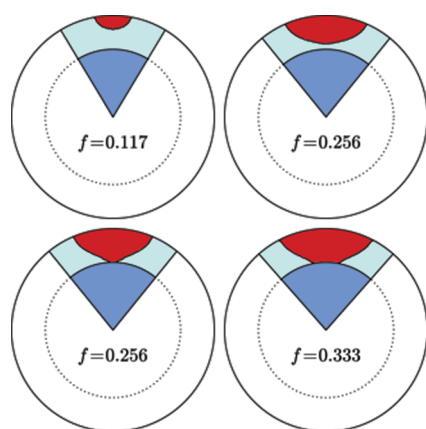
Figure 7. Evolution of the dot morphology as the diblock composition, f, changes at fixed segregation, $\chi N = 40$, highlighting the discontinuous transition that occurs at $f = 0.256$.

examined by Vorselaars et al.[42] using the full SCFT. By comparing our boundaries between the four morphology types with theirs (shown with arrows at the top of the diagram), we can see that the UCA has become less accurate for small particles. Nevertheless, it still remains a reasonable approximation.

Figure 5 shows one further phase diagram analogous to that of Figure 3, but for a nanoparticle of $R_c = aN^{1/2}$ rather than a flat substrate. The phase boundaries separating the uniform, dot, stripe, and hole morphologies (solid curves) are shifted toward larger f relative to those of the flat brush, in accordance with the trends observed in Figure 3 and rationalized by eq 1. Another difference is that the four morphology types no longer all meet at a critical point, which was marked by a solid dot in Figure 2; the reason for this will be explained in the Discussion. Again, the finite area of the spherical film leads to additional transitions (dashed curves), whenever a morphology undergoes a change in the number of its surface domains.

The natural tendency for domains to grow in size as the tension of the A/B interface increases implies that the n-dot, m:n-stripe, and n-hole phases should be ordered such that the number of domains (i.e., m and n) decreases with increasing χN; this is clearly the case. Vorselaars et al.[42] also argued that the number of domains should decrease with increasing f, based on the fact that the calculations for flat substrates[27] found that domain size increases with f. This implies that the dashed boundaries should have a negative slope, which is true apart from a portion of the hole region next to the stripe phase. As a result, the number of holes can increase and then decrease as one scans across f at constant χN.

To explain this nonmonotonic change in the number of holes, Figure 6 examines how the preferred domain size is affected by the diblock composition, f. We consider both the dot and hole phases, for which the domain size is defined on the outer air surface by $D = 2(R_c + L)\theta_{max}$. (The stripe phase is omitted from our consideration because the free energy of an individual stripe located at $\theta_{min} \leq \theta \leq \theta_{max}$ depends not only on its width, $D = (R_c + L)(\theta_{max} - \theta_{min})$, but also on its angular position, $(\theta_{max} + \theta_{min})/2$, on the sphere.) To access the preferred size of the dots and holes, we simply remove the constraint $\cos(\theta_{max}) = 1 - 2/n$, and instead determine the preferred value of θ_{max} by minimizing the free energy per chain. As observed earlier for flat substrates,[27] D generally increases with f, but for the spherical substrate (Figure 6b) there is also a substantial interval of the hole phase where D decreases slightly.

To gain further insight, we separate the domain size of the dots and holes into $D = d_A + d_B$, where d_A and d_B are the widths of the A- and B-rich regions, respectively (see Figure 6). As one would expect, d_A increases as the A block becomes longer and d_B decreases as the B block becomes shorter. However, the f-dependence of D depends crucially on which of d_A and d_B changes more rapidly. While d_A typically increases faster than d_B decreases producing a positive gradient in D, there are some exceptions.

One may notice that there is a small discontinuity in the domain spacing of the dot phase at $f = 0.256$ in Figure 6b. It is the result of a first-order phase transition involving a sudden change in the A/B interface, illustrated by Figure 7. As the size of the A-rich region grows, it eventually becomes advantageous for the dot to jump into contact with the spherical substrate so as to reduce the amount of A/B interface. The greater the A/B interfacial tension, the stronger the tendency for the dot to make contact with the substrate. Consequently the discontinuous transition, which is plotted in Figure 5 with a dotted curve, shifts toward smaller f with increasing χN. Because a stripe phase involves a dot at one or both of its poles, this transition also extends across the stripe region. Note that none of the actual stripes ever contact the substrate for the parameter values considered in this study.

■ DISCUSSION

As mentioned in the Results, the general shift of the laterally structured phases toward larger f, for spherical substrates (Figure 5) relative to the flat substrate (Figure 3), can be attributed to the fact that the lateral area of a spherical film increases toward the air surface, where the A-rich domains reside. It is also straightforward to explain the narrowing of the stripe region in Figure 5 with increasing χN. On a flat surface, the dot-to-stripe transition occurs as soon as it becomes energetically favorable to form stripes instead of dots. However, on a spherical surface, the stripe phase involves one or two polar dots, which dilutes the energetic advantage of switching to stripes. This is further exacerbated at high χN, because the larger domain size reduces the number of stripes, thus increasing the relative effect of the polar dots.

Another, more subtle, difference is the disappearance of the critical point. The stripe and hexagonal symmetries of the flat film converge to a critical point (denoted by a dot in Figure 3) in the exact same way as the lamellar, hexagonal, and bcc symmetries do in bulk systems.[47,52−55] (The critical point can be calculated with a single-harmonic Landau expansion analogous to that of Leibler for bulk melts,[56] but about the uniform phase instead of a homogeneous disordered phase.) However, the critical point vanishes for spherical substrates, because of the finite surface area and the loss of translational symmetry. For instance, A-rich stripes near the equator differ somewhat from those near the poles. Although the UCA removes this spatial variation from the dot and hole phases, the finite area still prevents the domains from acquiring their preferred size and this is also enough to destroy the critical point. Nevertheless, the point where the dot, hole, and uniform phases meet is nearly a critical transition, and thus we can still expect the dots and holes to be of similar size there;[27] indeed, we find that $n = 14$ for both phases.

Figures 3 and 4 demonstrate the small quantitative inaccuracies of the UCA. It is also informative and not too difficult to understand the general qualitative effect on the SCFT
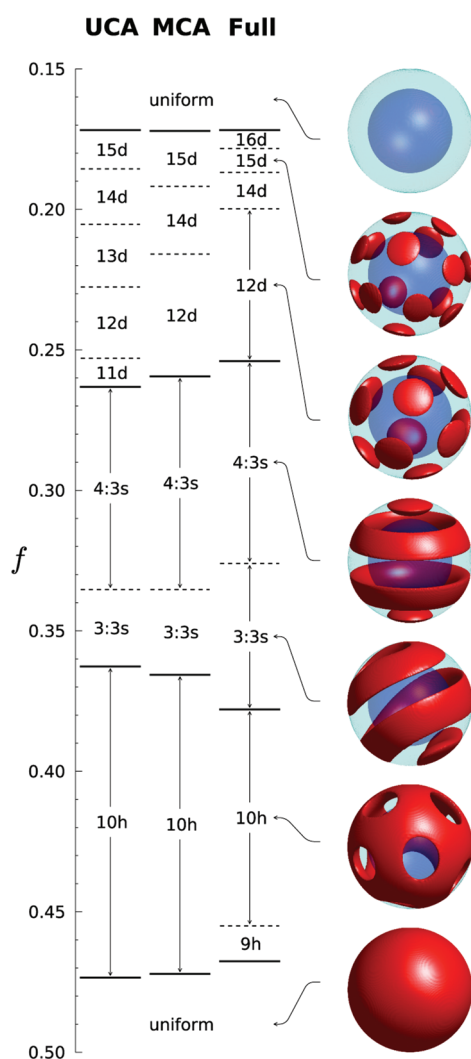
UCA MCA Full

Figure 8. Comparison of our UCA predictions for the phase boundaries with those from the MCA proposed by Chantawansri et al.[38] and the full SCFT calculation by Vorselaars et al.[42] for diblock copolymers of $\chi N = 25$ grafted to a core of radius $R_c = aN^{1/2}$.

predictions. In the case of the flat substrate, approximating the hexagonal unit cells of the dot and hole phases by circular cells relieves their *packing frustration*,[59,60] and thus lowers their free energy. This is why the dot and hole regions in Figure 3 are slightly larger for the UCA calculation (solid curves) as compared to the full SCFT calculation (dashed curves). This effect also carries over to the spherical brushes as illustrated in Figure 8, where we compare our UCA calculations to the full calculation of Vorselaars et al.[42] for a spherical substrate of radius $R_c = aN^{1/2}$.

The packing frustration, whereby the finite surface area forces domains to deviate from their preferred size, has an interesting effect on the stripe morphology that our 2D calculation fails to capture. The transition from the 4:3- to the 3:3-stripe phase causes the stripes to expand well beyond their preferred width. In the full 3D calculation, the 3:3-stripe phase is able to reduce the width of its stripes by deforming its polar dot and hole from circles to oblong shapes, which breaks the rotational symmetry. The resulting decrease in free energy shifts its phase boundary with the 4:3-stripe phase toward smaller *f*, as illustrated in Figure 8. An alternative way of modifying the width of the A-rich

domains is to form a spiral phase, but we suspect that this only becomes favorable for larger R_c.[38,42]

Packing frustration can also be used to explain the variations in the boundaries separating the different *n*-dot (or *n*-hole) phases. In the full SCFT calculation, the Voronoi cells of the *n* dots (or holes) will have a range of shapes and sizes, whereas they would prefer circular cells of the same size, as assumed in the UCA. Naturally, the level of packing frustration will be highly dependent on *n*. The 12-dot phase has a very low degree of packing frustration, because all 12 of its Voronoi cells are identical. In general though, the *n* cells of a *n*-dot phase are forced to adopt a range of sizes and shapes in order to fill space, which leads to a higher level of packing frustration. This explains the large 12-dot region and the omission of a 13-dot phase predicted by the full SCFT calculation in Figure 8. In the absence of packing frustration, the UCA predicts similar sized regions for each of the *n*-dot phases. By understanding this, we can deduce, for example, that the 10-hole phase has more packing frustration than the 9-hole phase given that the 10-hole region expands when the UCA is applied.

Chantawansri et al.[38] have attempted to incorporate some of the packing frustration back into the UCA for the dot phase, by accounting for the fact that the different dots have different numbers of neighbors. To do this, they assumed that the number of dots with *i* neighbors, n_i, for a given $n = \Sigma_i n_i$ is the same as that of the classic Thomson problem, where electrons are placed on a sphere so as to minimize the electrostatic energy. They still used circular cells, but with different areas. In particular, they assumed that the area of a cell is proportional to its number of neighbors. Figure 8 compares this multicell approximation (MCA) to our UCA and the full SCFT. While the MCA does correctly predict a large 12-dot region that wipes out the 13-dot phase, it fails to improve other aspects of the phase diagram, such as the missing 9-hole phase, and it makes some things worse, such as the boundary between the 14- and 15-dot phases. This is not entirely surprising; there is no reason that the cell size should depend solely on the number of neighbors, especially in a linear way. Therefore, we favor our simpler UCA, where each dot (or hole) is allocated an equal area.

The main advantage of the UCA is the resulting increase in computational speed compared to the full SCFT calculation by Vorselaars et al.[42] Even though we typically use 4 times their spatial resolution and 2.5 times the number of grid points along the chain contour, our algorithm takes around 0.2 s (using a single core of a 2.6 GHz Intel processor) to perform one Anderson-mixing iteration of the field equations as compared to 8 s for the full SCFT. More importantly, our calculation remains fast as the particle size increases. The time required to solve for the dot and hole phases is, in fact, unaffected by the particle size. The computational cost of the stripe phase does admittedly increase linearly with circumference and thus scales as R_c, but nevertheless, this is far better than the $R_c^3 \ln(R_c)$ scaling of the full SCFT calculation.[43]

Without the UCA and the assumption of rotational symmetry, phase diagrams like that of Figure 5 would represent a huge computational task, and this is just for neutral surfaces with one combination of *L* and R_c. Actual experiments will involve many additional parameters. It has already been shown that an affinity of the air surface for one of the polymer components has a sizable influence on the phase boundaries.[11,27] Likewise, the surface affinity of the substrate will affect the phase transition shown in Figure 7 and plotted in Figure 5 (dotted curve). Furthermore, if

we relax the assumption of a spherical air surface and allow its topography to adjust[57] under a finite polymer/air surface tension, this will add yet another parameter. Fortunately the UCA with 2D symmetry makes it feasible to explore large parameter spaces.

One could be concerned that the UCA might be very restrictive. However, experience has proven that the UCA is widely applicable among bulk systems thanks to the fact that the lamellar, cylindrical, and spherical morphologies remain the dominant phases for virtually all two-component block copolymer systems.[52−55] Only when the block copolymers acquire a third chemically distinct component does the phase diagram become populated with morphologies that are too complex for the UCA.[58] We can expect a similar degree of applicability for block copolymer films, and in particular it could equally well be used for binary mixed brushes.

As pointed out by Vorselaars et al.,[42] however, the SCFT is only applicable to particles with a sufficient number of grafted chains (i.e., more than 10^3).[42] Contrary to the predictions of mean-field theory, finite systems do not exhibit true phase transitions. Nevertheless, there will still be sharp crossovers between morphologies provided that the difference in their free energies, relative to k_BT, varies rapidly with respect to changes in the system parameters (e.g., f and χN). The more molecules that are involved, the sharper will be the crossovers between morphologies.

■ SUMMARY

In this study, self-consistent field theory (SCFT) was used to model a melt brush of diblock copolymers grafted to a spherical core (see Figure 1). The equilibrium phase behavior was investigated as a function of the diblock composition, f, the diblock segregation, χN, and the radius of the core, R_c, at a fixed brush thickness of $L = 0.5aN^{1/2}$ assuming the air and core surfaces are neutral. This is the same system examined earlier for a flat substrate ($R_c = \infty$) by Matsen and Griffiths[27] and for a spherical substrate ($R_c = aN^{1/2}$) by Vorselaars et al.[42] Our new study, however, implements a unit-cell approximation (UCA) for the dot and hole phases and is limited to stripe phases with rotational symmetry (see Figure 2). This increases the speed of the calculation by orders of magnitude over that of the full SCFT calculation developed by Vorselaars et al., particularly for larger particles.

Although some accuracy is lost with the UCA, our SCFT calculation allows one to map out phase behavior over large parameter spaces while still retaining the detail of a microscopic theory. Most of the behavior, such as the general trend in the phase boundaries, the size of the domains, and the discontinuous transitions where the end-block domains jump into contact with the substrate, is adequately captured by the UCA. The only real shortcoming of the UCA is that it omits the effects of packing frustration, which become important for small particles. However, in this limit, there is always the option of following up the UCA calculation by a full SCFT calculation. In fact, by comparing the two calculations, one gains a quantitative understanding of the packing frustration effects, which is not possible from either calculation on its own.

We anticipate that our SCFT algorithm will provide a useful tool for the future development of patterned nanoparticles. It can be readily adapted to a wide range of systems, including the mixed brushes that are currently receiving considerable experimental attention.[15−20] With its computational speed, researchers will be able to scan their large parameter spaces to anticipate effects of, for example, varying particle size, changing the surface affinities or adding solvents, in order to guide their experimental studies.

■ AUTHOR INFORMATION

Corresponding Author

*E-mail: (G.H.G.) guy.griffiths@reading.ac.uk; (M.W.M.) m.w.matsen@reading.ac.uk.

■ ACKNOWLEDGMENT

■ REFERENCES

(1) Minko, S.; Müller, M.; Usov, D.; Scholl, A.; Froeck, C.; Stamm, M. *Phys. Rev. Lett.* **2002**, *88*, 035502.

(2) Minko, S.; Luzinov, I.; Luchnikov, V.; Müller, M.; Patil, S.; Stamm, M. *Macromolecules* **2003**, *36*, 7268−7279.

(3) Lemieux, M.; Usov, D.; Minko, S.; Stamm, M.; Shulha, H.; Tsukruk, V. V. *Macromolecules* **2003**, *36*, 7244−7255.

(4) Lemieux, M. C.; Julthongpiput, D.; Bergman, K. N.; Cuong, P. D.; Ahn, H.-S.; Lin, Y.-H.; Tsukruk, V. V. *Langmuir* **2004**, *20*, 10046−10054.

(5) Usov, D.; Gruzdev, V.; Nitschke, M.; Stamm, M.; Hoy, O.; Luzinov, I.; Tokarev, I.; Minko, S. *Macromolecules* **2007**, *40*, 8774−8783.

(6) Motornov, M.; Sheparovych, R.; Katz, E.; Minko, S. *ACS Nano* **2008**, *2*, 41−52.

(7) Zhao, B.; Bittain, W. J.; Zhou, W.; Cheng, S. Z. D. *Macromolecules* **2000**, *33*, 8821−8827.

(8) Tomlinson, M. R.; Genzer, J. *Langmuir* **2005**, *21*, 11552−11555.

(9) Gao, X.; Feng, W.; Shiping, Z.; Sheardown, H.; Brash, J. L. *Langmuir* **2008**, *24*, 8303−8308.

(10) Akgun, B.; Ugur, G.; Brittain, W. J.; Majkrzak, C. F.; Li, X. F.; Wang, J.; Li, H. M.; Wu, D. T.; Wang, Q.; Foster, M. D. *Macromolecules* **2009**, *42*, 8411−8422.

(11) O'Driscoll, B. M. D.; Griffiths, G. H.; Matsen, M. W.; Perrier, S.; Ladmiral, V.; Hamley, I. W. *Macromolecules* **2010**, *43*, 8177−8184.

(12) Dai, S.; Ravi, P.; Tam, K. C. *Soft Matter* **2009**, *5*, 2513−2533.

(13) Uhlmann, P.; Merlitz, H.; Sommer, J. U.; Stamm, M. *Macromol. Rapid Commun.* **2009**, *30*, 732−740.

(14) Motornov, M.; Roiter, Y.; Tokarev, I.; Minko, S. *Prog. Polym. Sci.* **2010**, *35*, 174−211.

(15) Li, D.; Sheng, X.; Zhao, B. *J. Am. Chem. Soc.* **2005**, *127*, 6248−6256.

(16) Zhao, B.; Zhu, L. *J. Am. Chem. Soc.* **2006**, *128*, 4574−4575.

(17) Zhu, L.; Zhao, B. *J. Phys. Chem. B* **2008**, *112*, 11529−11536.

(18) Zhao, B.; Zhu, L. *Macromolecules* **2009**, *42*, 9369−9383.

(19) Jiang, X.; Zhong, G.; Horton, J. M.; Jin, N.; Zhao, B. *Macromolecules* **2010**, *43*, 5387−5395.

(20) Jiang, X.; Zhao, B.; Zhong, G.; Horton, J. M.; Zhu, L.; Hafner, R. S.; Lodge, T. P. *Macromolecules* **2010**, *43*, 8209−8217.

(21) Pyun, J.; Matyjaszewski, K.; Kowalewski, T.; Savin, D.; Patterson, G.; Kickelbick, G.; Huesing, N. *J. Am. Chem. Soc.* **2001**, *123*, 9445−9446.

(22) Marko, J. F.; Witten, T. A. *Phys. Rev. Lett.* **1991**, *66*, 1541−1544.

(23) Zhulina, E. B.; Balazs, A. C. *Macromolecules* **1996**, *29*, 2667−2673.

(24) Zhulina, E. B.; Singh, C.; Balazs, A. C. *Macromolecules* **1996**, *29*, 6338−6348.

(25) Zhulina, E. B.; Singh, C.; Balazs, A. C. *Macromolecules* **1996**, *29*, 8254−8259.

(26) Müller, M. *Phys. Rev. E* **2002**, *65*, 030802.

(27) Matsen, M. W.; Griffiths, G. H. *Eur. Phys. J. E* **2009**, *29*, 219–227.

(28) Brown, G.; Chakrabarti, A.; Marko, J. F. *Europhys. Lett.* **1994**, *25*, 239–244.

(29) Yin, Y. H.; Sun, P. C.; Li, B. H.; Chen, T. H.; Jin, Q. H.; Ding, D. T.; Shi, A.-C. *Macromolecules* **2007**, *40*, 5161–5170.

(30) Wang, J.; Müller, M. *J. Phys. Chem. B* **2009**, *113*, 11384–11402.

(31) Wang, J.; Müller, M. *Macromolecules* **2009**, *42*, 2251–2264.

(32) Wang, J.; Müller, M. *Langmuir* **2009**, *26*, 1291–1303.

(33) Guskova, O. A.; Seidel, C. *Macromolecules* **2011**, *44*, 671–682.

(34) Matsen, M. W. In *Soft Matter: Polymer Melts and Mitures*; Gompper, G., Schick, M., Eds.; Wiley-VCH: Weinheim, Germany, 2006; Vol. 1, Chapter 2.

(35) Fredrickson, G. H. *The Equilibrium Theory of Inhomogeneous Polymers*; Oxford University Press: New York, 2006.

(36) Meng, D.; Wang., Q. *J. Chem. Phys.* **2009**, *130*, 134904.

(37) Li, J. F.; Fan, J.; Zhang, H. D.; Qiu, F.; Tang, P.; Yang, Y. L. *Eur. Phys. J. E* **2006**, *20*, 449–457.

(38) Chantawansri, T. L.; Bosse, A. W.; Hexemer, A.; Ceniceros, H. D.; Garca-Cervera, C. J.; Kramer, E. J.; Fredrickson, G. H. *Phys. Rev. E* **2007**, *75*, 031802.

(39) Lishchuk, S. V. *J. Phys. A: Math. Theor.* **2009**, *42*, 465401.

(40) Roan, J.-R. *Int. J. Mod. Phys. B* **2004**, *18*, 2469–2475.

(41) Roan, J.-R. *Phys. Rev. Lett.* **2006**, *96*, 248301.

(42) Vorselaars, B.; Kim, J. U.; Chantawansri, T. L.; Fredrickson, G. H.; Matsen, M. W. *Soft Matter* **2011**, *7*, 10.1039/COSM01242D.

(43) The calculation involves transformations between a real-space mesh and the spherical harmonics, $Y_{\ell m}(\theta,\varphi)$, for $\ell \leq \ell_{max}$. The required number of harmonics increases as $\ell_{max} \propto R_c$, and the computational cost of the transformation routine used by Vorselaars et al.[42] scales as $\ell_{max}^{\nu}\ln(\ell_{max})$ with an exponent of $\nu = 3$, although new algorithms have been developed with $\nu = 2$.

(44) Helfand, E.; Wasserman, Z. R. *Macromolecules* **1978**, *11*, 960–966.

(45) Helfand, E.; Wasserman, Z. R. *Macromolecules* **1980**, *13*, 994–998.

(46) Semenov, A. N. *JETP* **1985**, *61*, 733–742.

(47) Vavasour, J. D.; Whitmore, M. D. *Macromolecules* **1992**, *25*, 5477–5486.

(48) Matsen, M. W. *Macromolecules* **2003**, *36*, 9647–9657.

(49) Matsen, M. W. *Eur. Phys. J. E* **2010**, *33*, 297–306.

(50) Kim, J. U.; Matsen, M. W. *Macromolecules* **2008**, *41*, 4435–4443.

(51) Matsen, M. W. *Eur. Phys. J. E* **2009**, *30*, 361–369.

(52) Matsen, M. W.; Schick, M. *Macromolecules* **1994**, *27*, 6761–6767.

(53) Matsen, M. W.; Schick, M. *Macromolecules* **1994**, *27*, 7157–7163.

(54) Matsen, M. W. *Macromolecules* **1995**, *28*, 5765–5773.

(55) Matsen, M. W.; Thompson, R. B. *J. Phys. Chem.* **1999**, *111*, 7139–7146.

(56) Leibler, L. *Macromolecules* **1980**, *13*, 1602–1617.

(57) Kim, J. U.; Matsen, M. W. *Soft Matter* **2009**, *5*, 2889–2895.

(58) Bates, F. S.; Fredrickson, G. H. *Phys. Today* **1999**, *52*, 32–38.

(59) Matsen, M. W.; Bates, F. S. *Macromolecules* **1996**, *29*, 7641–7644.

(60) Matsen, M. W. *J. Phys.: Condens. Matter* **2002**, *14*, R21–R47.